crystals

MDPI

Article

Optimization of Parameters in Laser Powder Bed Fusion TA15 Titanium Alloy Using Taguchi Method

Yang Liu [1,2,*], Zichun Wu [1], Qing Wang [3], Lizhong Zhao [3], Xichen Zhang [1], Wei Gao [1], Jing Xu [1], Yufeng Song [1,*], Xiaolei Song [4,*] and Xuefeng Zhang [3]

1 Hunan Engineering Research Center of Forming Technology and Damage Resistance Evaluation for High Efficiency Light Alloy Components, School of Mechanical Engineering, Hunan University of Science and Technology, Xiangtan 411201, China
2 National Key Laboratory of Science and Technology on High-Strength Structural Materials, Central South University, Changsha 410083, China
3 Institute of Advanced Magnetic Materials, College of Materials and Environmental Engineering, Hangzhou Dianzi University, Hangzhou 310018, China
4 Key Laboratory of Advanced Structural Materials, Ministry of Education, College of Materials Science and Engineering, Changchun University of Technology, Changchun 130012, China
* Correspondence: liuyang7740038@163.com (Y.L.); federer.song@163.com (Y.S.); songxiaolei@ccut.edu.cn (X.S.)

Abstract: In this work, laser powder bed fusion (LPBF) was explored to fabricate TA15 (Ti-6Al-2Zr-1Mo-1V) titanium alloy based on the experimental design obtained by using the Taguchi method. The impact of processing parameters (including laser power, scanning speed, and scanning interval) on the density and microhardness of the as-LPBFed TA15 titanium alloy was analyzed using the Taguchi method and analysis of variance (ANOVA). The interaction among parameters on the density of the as-LPBFed TA15 titanium alloy was indicated by a response surface graph (RSR). When the laser energy density was adjusted to 100 J/mm^3, the highest relative density could reach 99.7%. The further increase in the energy input led to the reduction in relative density, due to the formation of tiny holes caused by the vaporization of material at a high absorption of heat. Furthermore, in order to better reveal the correlation between relative density and processing parameters, the regression analysis was carried out for relative density. The results showed that the experimental and predicted values obtained by the regression equation were nearly the same.

Keywords: laser-based powder bed fusion; titanium alloy; Taguchi; process optimization; density

Citation: Liu, Y.; Wu, Z.; Wang, Q.; Zhao, L.; Zhang, X.; Gao, W.; Xu, J.; Song, Y.; Song, X.; Zhang, X. Optimization of Parameters in Laser Powder Bed Fusion TA15 Titanium Alloy Using Taguchi Method. *Crystals* **2022**, *12*, 1385. https://doi.org/10.3390/cryst12101385

Academic Editors: Yang Zhang, Shouxun Ji and Yuqiang Chen

Received: 28 August 2022
Accepted: 26 September 2022
Published: 29 September 2022

1. Introduction

TA15 (Ti-6Al-2Zr-1Mo-1V) titanium alloy is a high-aluminum-equivalent α titanium alloy, which has good specific strength, high-temperature creep resistance, thermal stability, and corrosion resistance. This alloy has also been widely used in the key load-bearing components and engine structure parts of aerospace applications [1–3]. However, titanium alloy has high activity, low thermal conductivity, and high deformation resistance [4–7], which makes it very difficult to manufacture by traditional manufacturing methods, such as casting [8,9], forging [10,11], and welding [12–14]. In addition, aerospace parts tend to be functional, lightweight, and have a structural integrated design [15–23]. Meanwhile, it is increasingly difficult for traditional manufacturing technology to meet the manufacturing needs of aerospace titanium alloy parts with complex structures. Hence, new types of manufacturing techniques should be explored to fabricate the complex structures.

Metal additive manufacturing (AM) techniques, including laser powder bed fusion (LPBF) [24–26] and laser powder deposition (LPD) [27–29], have been confirmed to successfully fabricate complex structures of titanium alloy parts. Compared with others, research has mainly concentrated on the directed-energy-deposition-fabricated TA15 titanium alloy [30,31], which can directly fabricate the large-scale complex structural components.

However, in order to obtain the TA15 structural parts with higher precision, some studies have conducted research on LPBF-processed TA15 titanium alloy. Laser powder bed fusion is a promising metal AM technique that utilizes a focused laser beam to selectively melt metal powder layer by layer under the guidance of a computer-aided-design (CAD) model [3,6]. It has the advantages of high material utilization rate, high precision, and directly manufacturing near-full-density complex-shaped metal parts [32], which indicates that the application of LPBF to manufacture TA15 titanium alloy parts has the potential to extend its application in aerospace [33]. However, the characteristics of high-temperature melting and rapid solidification in the LPBF process may result in some issues [34,35]. For example, the evaporation of elements in the heating process and the volume shrinkage in the cooling process both easily lead to pore generation [36]. There is even a lack of fusion defects existing due to improper adjustment of process parameters [37]. These pores and lack of fusion will reduce the relative density of LPBF-fabricated metal parts, resulting in seriously degrading the mechanical properties [38]. Therefore, achieving a high density of LPBF-fabricated metal parts has become a target for researchers.

As for LPBF Ti-Al-Zr-Mo-V titanium alloy, Li et al. [3] investigated the effect of LPBF process parameters on the relative density of the TA15 titanium alloy sample, and found that the volume energy density (E_v) range of 125–167 J/mm^3 is the optimal LPBF process window for manufacturing high-density TA15 titanium alloy. At the same time, Li et al. [39] also reported that the effect of the different levels of scanning strategies on the relative density of LPBF-fabricated TA15 titanium alloy caused a significant difference. Thijs et al. [40] systematically investigated the correlation between the density of Ti6Al4V and various parameters via experiments and simulation, but did not consider the effect of parameter–parameter interactions on the density.

The Taguchi method has been proven to be a powerful means to optimize multiple parameters with the consideration of the interaction among process parameters [41–43]. Kumar et al. [44] investigated the effect of wire electrical discharge machining (WEDM) process parameters on the rate of material removal (MRR), surface roughness (SR), and corrosion rate (CR) of ZE41A magnesium alloy using the Taguchi method, and determined the optimized parameter combinations of each of them based on considering the interaction among process parameters. Pandel et al. [45] reported the influence of input parameters (including cross-sectional area and TE leg length) on the output parameter (power output of Mg2(Si–Sn) thermoelectric generators) using the Taguchi method, and the contributions of each parameter were obtained by ANOVA analysis with the results of 35.22% and 27.62%, respectively. In our study, adopting the Taguchi method can minimize the number of experiments required to achieve a fuller understanding of the effects of processing parameters on the relative density of LPBF-fabricated TA15 titanium alloy. In addition, according to the Taguchi experimental design, the optimized parameters can be obtained by the approach that compares the mean of the signal-to-noise (S/N) ratio. The important parameters and percentage contribution of the single process parameter on density were obtained by ANOVA.

In this work, the Taguchi method was utilized to optimize LPBF process parameters targeting high-density TA15 titanium alloy samples. The effect of laser energy density on the relative density of the as-LPBFed TA15 titanium alloy was discussed. The optimized parameter results were validated by confirmation analysis. This work aimed to provide the database and guidance for LPBF fabrication of TA15 titanium alloy.

2. Materials and Methods

2.1. Materials

The gas-atomized TA15 titanium alloy powder used in this work was purchased from Avimetal Powder Metallurgy Technology Co., Ltd., China. The chemical composition of TA15 titanium alloy powder is listed in Table 1. The main alloying elements of TA15 titanium alloy are Al, V, Zr, Mo, and Ti, as indicated in Table 1. The morphology and size distribution of TA15 titanium alloy powder are presented in Figure 1. The powder particles were spherically shaped with an equivalent spherical diameter of 15–53 μm (D10 = 21.46 μm, D50 = 33.73 μm, and D90 = 48.50 μm).

Table 1. Chemical composition (Wt. %) of the TA15 titanium alloy powder.

Elements	Al	V	Zr	Mo	Si	Fe	Ti
TA15	6.42	1.94	1.93	1.43	0.02	0.03	Balance

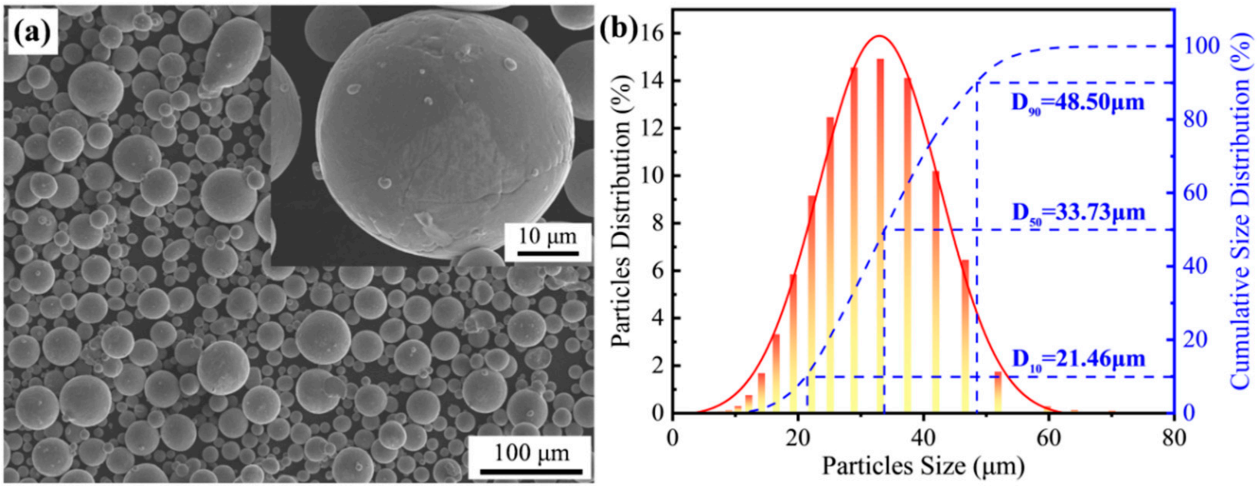

Figure 1. Morphology (**a**) and size distribution (**b**) of TA15 titanium alloy powder.

2.2. Sample Fabrications and Optimization of Parameters Using Taguchi Method

The LPBF experiments were carried out by a DiMetal-100 3D printing machine (Guangzhou Leijia Additive Technology Co., Ltd., Guangzhou, China) with an oxygen concentration below 100 ppm. High density is the premise for the sample to have excellent mechanical properties, and the density of the LPBF-fabricated TA15 titanium alloy was largely affected via process parameters, such as laser power, laser scanning speed, scanning interval, and powder-bed layer thickness.

In this investigation, the Taguchi method was utilized to optimize the parameters for the density of the LPBF-fabricated TA15 titanium alloy. Based on a previous study on the effect of laser energy density on the densification of titanium alloy [46] and the fact that the low power was expected to obtain a satisfactory surface quality, the regions of the process parameters were determined. The three controllable five-level process parameters are listed in Table 2. Considering the interaction among parameters, the experimental parameters combinations were determined by the orthogonal test method using the Taguchi method. An L_{25} orthogonal array was obtained as shown in Table 3 using MINITAB statistical software (MINITAB 16, Pennsylvania State University, Pennsylvania, USA). The 25 parametric combinations listed in Table 3 were then applied to fabricate 10 $\times$ 10 $\times$ 10 mm^3 cubes for the sake of parametric optimization. The experimental results are displayed in the form of S/N ratio, which could be separated from the three types of performance features: nominal-the-better, smaller-the-better, and larger-the-better. In this study, the objective was to obtain maximum density in the LPBF-fabricated TA15 titanium alloy. Thereafter, the larger-the-better feature was chosen. The larger-the-better S/N ratio can be obtained based on the following equation:

$$\frac{\mathrm{S}}{\mathrm{N}} = -10 \log\left(\frac{1}{n}\sum_{i=1}^{n}\frac{1}{y_i^2}\right) \quad (1)$$

where y_i refers to the value of density for the ith experiment, and n represents the total number of experiments.

Table 2. The process parameters and their levels used in this study.

Parameters	Level 1	Level 2	Level 3	Level 4	Level 5
A: Laser power (W)	150	160	170	180	190
B: Scanning speed (mm/s)	800	900	1000	1100	1200
C: Scanning interval (mm)	0.06	0.07	0.08	0.09	0.10

Table 3. Experimental design as L_{25} orthogonal array and experimental results for relative density.

Runs	Laser Power (W)	Scanning Speed (mm/s)	Scanning Interval (mm)	Laser Energy Density (J/mm^3)	Microhardness ($HV_{0.1}$)	Relative Density (%)		
						Experimental Value	Predicted Value	Error (%)
1	150	800	0.06	107.64	365.56	99.46	99.26	−0.2007
2	150	900	0.07	79.36	336.00	98.96	99.10	0.1437
3	150	1000	0.08	62.5	350.66	98.78	98.77	−0.0138
4	150	1100	0.09	50.51	321.18	98.32	98.25	−0.0681
5	150	1200	0.10	41.67	319.53	97.74	97.56	−0.1821
6	160	800	0.07	95.24	347.96	99.52	99.30	−0.2206
7	160	900	0.08	74.07	327.26	99.26	99.12	−0.1384
8	160	1000	0.09	59.26	353.04	98.79	98.75	−0.0376
9	160	1100	0.10	48.48	324.46	98.24	98.19	−0.0497
10	160	1200	0.06	74.07	328.90	99.18	99.01	−0.1746
11	170	800	0.08	88.54	327.84	99.43	99.32	−0.1068
12	170	900	0.09	69.96	331.06	99.08	99.11	0.0323
13	170	1000	0.10	56.67	327.00	99.02	98.69	−0.3292
14	170	1100	0.06	85.86	326.94	99.37	99.3	−0.0620
15	170	1200	0.07	67.46	328.96	99.36	98.99	−0.3688
16	180	800	0.09	84.51	322.14	99.62	99.33	−0.2907
17	180	900	0.10	66.67	322.50	99.43	99.07	−0.3617
18	180	1000	0.06	100	317.46	99.7	99.43	−0.2746
19	180	1100	0.07	77.92	329.76	99.19	99.28	0.0872
20	180	1200	0.08	62.5	317.50	99.14	98.91	−0.2359
21	190	800	0.10	79.17	318.70	99.2	99.32	0.1214
22	190	900	0.06	117.28	330.66	99.37	99.36	−0.0099
23	190	1000	0.07	90.48	324.74	99.64	99.39	−0.2509
24	190	1100	0.08	71.97	317.10	99.15	99.18	0.0351
25	190	1200	0.09	58.64	308.12	98.83	98.74	−0.0864

Finally, the percent contribution of each parameter and significant parameters for the density were obtained by the method of analysis of variance (ANOVA).

2.3. Characterizations

Inductively coupled plasma-atomic emission spectrometry (ICP-AES) was employed to determine the chemical component of TA15 titanium alloy powder. Scanning electron microscopy (Nova Nano SEM230) was performed for the morphology of TA15 titanium alloy powder. The size distribution of TA15 titanium alloy powder was counted by a laser particle size analyzer (Mastersizer 3000). The microstructure of the LPBF-fabricated TA15 titanium alloy samples was characterized by a scanning electron microscope (Nova Nano SEM230) using back-scattered mode (SEM-BSE).

The Archimedes principle was used to measure the relative density of LPBF-fabricated TA15 titanium alloy samples, and the results were indicated with a percentage of the TA15 titanium alloy density (4.45 g/cm^3) [47]. To decrease the randomness of the tests, five measurements were carried out for every sample, and the mean of the measurements was represented as the experimental value of the relative density. The vertical section (X–Y plane) of each sample was polished for Vickers microhardness tests and the tests were conducted by a digital microhardness instrument at a load of 100 g and a dwell time of 10 s. The results obtained for each set of samples were the average values of at least three measurements.

3. Results and Discussion

3.1. Effect of Processing Parameters on Density and Microhardness of as-LPBFed TA15 Titanium Alloy

3.1.1. Effects of Laser Power

Figure 2 shows the effect of laser power on the density and microhardness of the as-LPBFed TA15 titanium alloy. Here, the value of each bar represents the average value of the experimental results obtained by five parameter combinations under a certain level of laser power. It can be seen from Figure 2a that the relative density of the as-LPBFed TA15 titanium alloy was below 99% with an average value of 98.65% when the laser power was 150 W, but it was beyond 99% with the increase in laser power from 150 W to 170 W. The reason was that the low energy input corresponded to the low depth, width, and height of the molten pool, which was why some of the powders could not be fully melted in the LPBF process, resulting in the decrease in relative density, and the higher levels of laser power could melt more alloy powders in the molten pool to obtain higher relative density [48]. Subsequently, the laser power increased from 170 W to 180 W, further increasing the relative density. It is worth noticing that the relative density could reach up to 99.5% when the laser power was 180 W. However, the higher laser power of 190 W caused the decrease in relative density, which was owing to the excessive energy input to the elements by burning [41], resulting in a decreasing relative density of samples. Interestingly, as shown in Figure 2b, the samples of the lowest relative density indicated the highest microhardness, and the microhardness of these five levels of laser power from 150 W to 190 W represented a decreasing trend from 338.5 $HV_{0.1}$ to 319.8 $HV_{0.1}$, from which it could be indicated that the mechanical properties of samples were not only determined by relative density but also by many factors. Meanwhile, the values of the relative density exhibited a significant change when the laser power increased from 150 W to 190 W, which indicated the significant contribution of laser power to the relative density of LPBF TA15 alloys.

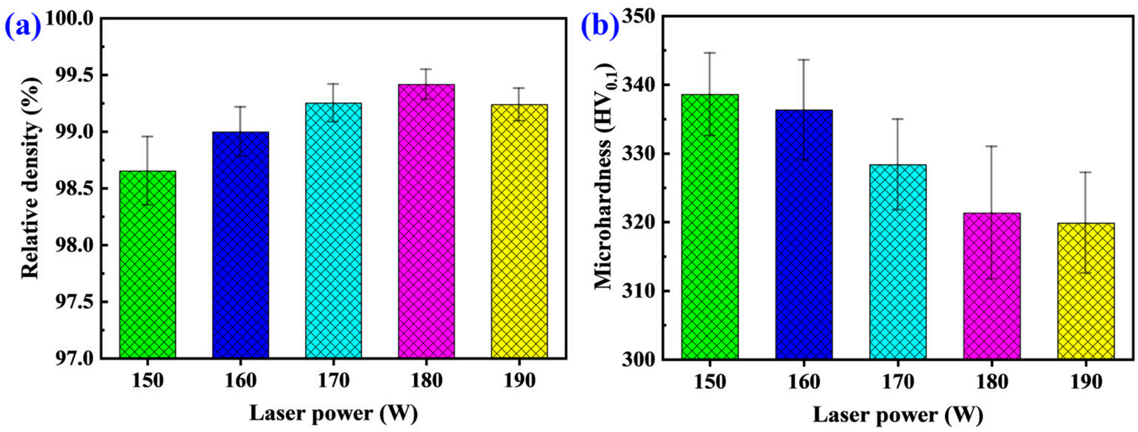

Figure 2. The density (**a**) and microhardness (**b**) of as-LPBFed TA15 titanium alloy under various laser powers.

3.1.2. Effects of Scanning Speed

Figure 3 shows the influence of scanning speed on the density and microhardness of the as-LPBFed TA15 titanium alloy. Here, the value of each bar represents the average value of experimental results obtained by five parameter combinations under a certain level of scanning speed. As the scanning speed increased from 800 mm/s to 1200 mm/s at an interval of 100 mm/s, the relative density of the as-LPBFed TA15 titanium alloy decreased from 99.44% to 98.85%, as shown in Figure 3a, which was due to the laser energy density decreasing as the scanning speed increased. Consequently, the generated molten pool caused by insufficient energy input could not fully catch the alloy powders, leading to the decrease in relative density [49]. Meanwhile, Figure 3b indicates the effect of scanning speed on the microhardness of the as-LPBFed TA15 titanium alloy, from which it could be seen that the trend of microhardness of the as-LPBFed TA15 titanium alloy was decreasing from 336.4 $HV_{0.1}$ to 329.4 $HV_{0.1}$ first upon the increase in scanning speed from 800 mm/s 900 mm/s. Then, the further increase in scanning speed from 900 mm/s to 1000 mm/s simultaneously improved the microhardness, and the microhardness reached 334.5 $HV_{0.1}$ when the scanning speed was 1000 mm/s. Then, the scanning speed increased from

1000 mm/s to 1200 mm/s, giving rise to a steep descent in microhardness from 334.5 $HV_{0.1}$ to 320.6 $HV_{0.1}$.

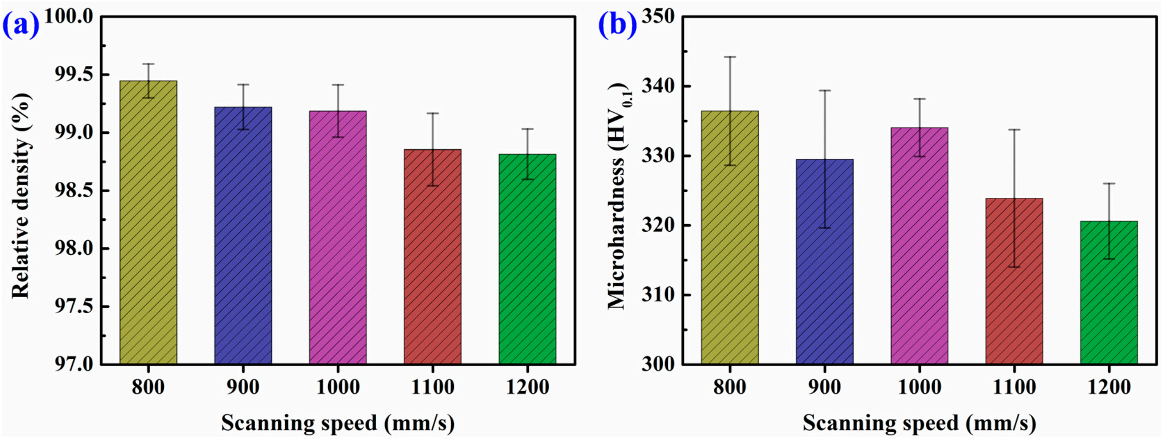

Figure 3. The density (**a**) and microhardness (**b**) of as-LPBFed TA15 titanium alloy under various scanning speeds.

3.1.3. Effects of Scanning Interval

Figure 4 shows the relationships between scanning interval and density and microhardness of the as-LPBFed TA15 titanium alloy. Here, the value of each bar represents the average value of experimental results obtained by five parameter combinations under a certain level of scanning interval. As the scanning interval increased from 0.06 mm to 0.10 mm with an interval of 0.01 mm, the density of the as-LPBFed TA15 titanium alloy decreased correspondingly from 99.41% to 98.72% with a smooth trend. The descent trend of density with increasing scanning interval was owing to the lower energy density per unit volume, leading to the decreasing energy adopted by the TA15 powders [41]. Meanwhile, the microhardness of the as-LPBFed TA15 titanium alloy also represented a reduction trend from 333.9 $HV_{0.1}$ to 322.4 $HV_{0.1}$ with the increase in scanning interval from 0.06 mm to 0.10 mm.

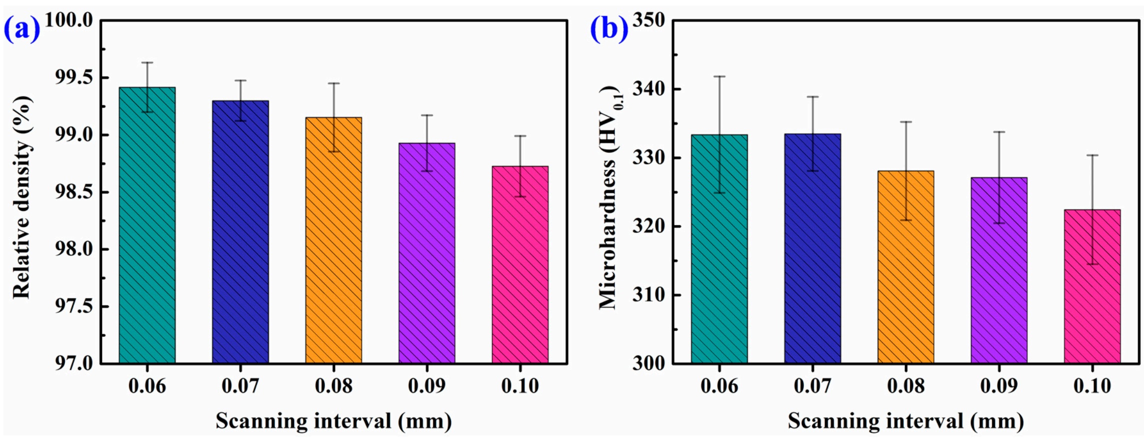

Figure 4. The density (**a**) and microhardness (**b**) of as-LPBFed TA15 titanium alloy under various scanning intervals.

3.2. Optimization of Parameters for Density

3.2.1. Analysis of the Signal-to-Noise (S/N) Ratio

The output parameter (relative density) was utilized to measure the mean and signal-to-noise ratios of every input parameter for the best quality of the as-LPBFed TA15 titanium alloy specimens. The mean value and signal-to-noise ratio (S/N) were obtained to evaluate the effect of every process parameter on the as-LPBFed TA15 titanium alloy specimens.

In this investigation, the larger the criterion, the better the model used to select the mean and S/N ratio to identify the response of the process parameters. Tables 4 and 5 show the response tables for relative density of the mean value and the signal-to-noise ratio, respectively. The larger the distinction between the S/N values, the more significant the process parameters were. Thus, it can be indicated that the laser power had the greatest effect on the relative density. In addition, the primary effect curves of the mean value and S/N ratio on the densities are shown in Figures 5 and 6. It can be seen that the highest relative density of the as-LPBFed TA15 titanium alloy specimens was obtained at the process parameters of laser power of 180 W, scanning speed of 800 mm/s, and scanning interval of 0.06 mm.

Table 4. Mean response table for relative density.

Level	Laser Power	Scanning Speed	Scanning Interval
1	98.65	99.45	99.42
2	99.00	99.22	99.33
3	99.25	99.19	99.15
4	99.42	98.85	98.93
5	99.24	98.85	98.73
Delta	0.76	0.60	0.69
Rank	1	3	2

Table 5. S/N ratio response table for relative density.

Level	Laser Power	Scanning Speed	Scanning Interval
1	39.88	39.95	39.95
2	39.91	39.93	39.94
3	39.93	39.93	39.93
4	39.95	39.90	39.91
5	39.93	39.90	39.89
Delta	0.07	0.05	0.06
Rank	1	3	2

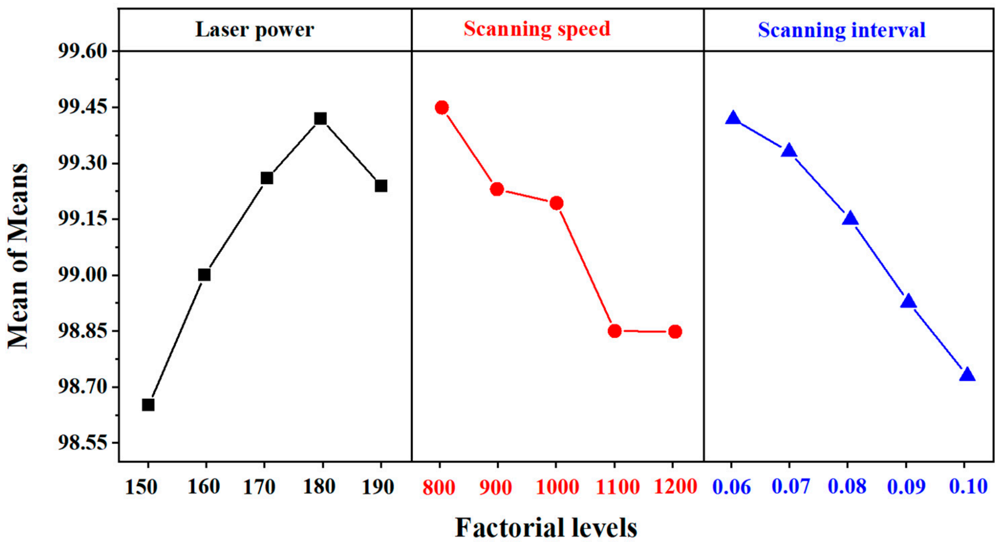

Figure 5. Main effect plots of means—relative density.

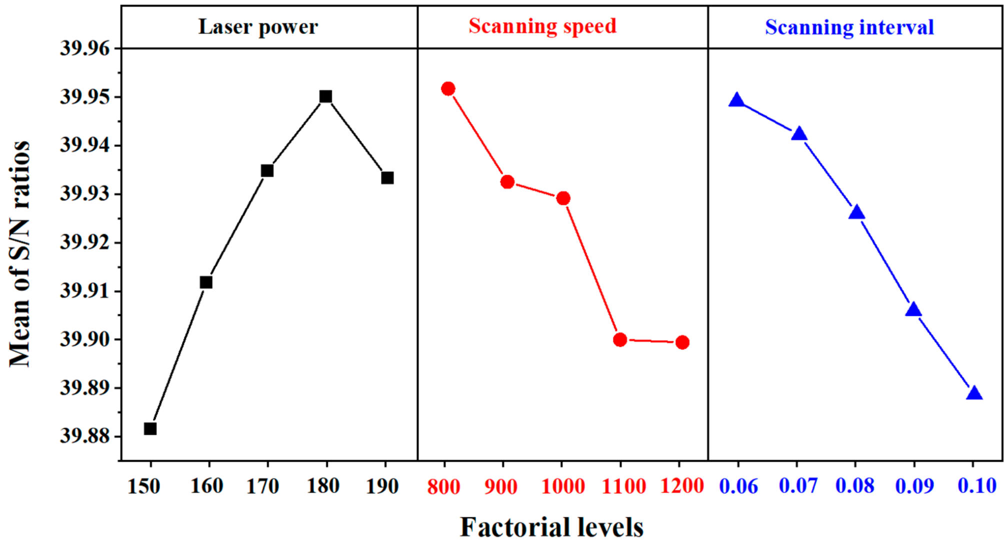

Figure 6. Main effect plots of S/N ratio—relative density.

3.2.2. Analysis of Variance (ANOVA)

The percentage contribution of every parameter was calculated by ANOVA. ANOVA facilitated the formal testing of the results of all the main factors and their relationships by assessing the mean squared deviation of the experimental error approximation at a defined confidence level. In this study, the percentage contribution of each process parameter to obtain the best molding quality of the specimen was performed by MINITAB software. The most significant process parameter obtained by calculating the percentage contribution was the laser power of 33.86%, followed by the scanning interval of 31.33% and finally the scanning speed of 25.35%. Table 6 indicates the results obtained by ANOVA of the densities. The results show that the laser power was the most significant process parameter affecting the relative density of the as-LPBFed TA15 titanium alloy.

Table 6. Results acquired from ANOVA—relative density.

Source	DF	Seq. SS	Adj. SS	Adj. MS	F	P	Percentage of Contribution (%)
Laser power	4	1.7624	1.7624	0.44061	10.72	0.001	33.86
Scanning speed	4	1.3195	1.3195	0.32988	8.03	0.002	25.35
Scanning interval	4	1.6307	1.6307	0.40769	9.92	0.001	31.33
Error	12	0.4930	0.4930	0.04108	—	—	9.47
Total	24	5.2057	—	—	—	—	100

DF, degree of freedom; Seq. SS, sequential sum of squares; Adj. SS, adjusted sum of squares; Adj. MS, adjusted mean squares; F, statistical test; P, statistical value [46].

3.3. *Effect of Laser Energy Density on Relative Density of as-LPBFed TA15 Titanium Alloy*

In this section, the interaction influences of scanning speed and laser power on the relative density of the alloy are discussed. Figure 7 shows the response surface graph and contour plot for the influence of laser power and scanning speed on the relative density obtained by using Design Expert software, from which it can be directly seen that the relative density of samples first increased obviously and then slightly reduced with the reduction in the scanning speed or the increase in the laser power. The effect of the scanning speed on relative density appeared more remarkable at lower laser powers, and so did laser power at high scanning speeds. As reported, volume energy density (E_v) is the critical element that determines the relative density, and it can be represented as follows:

$$E_v = P/vht \quad (2)$$

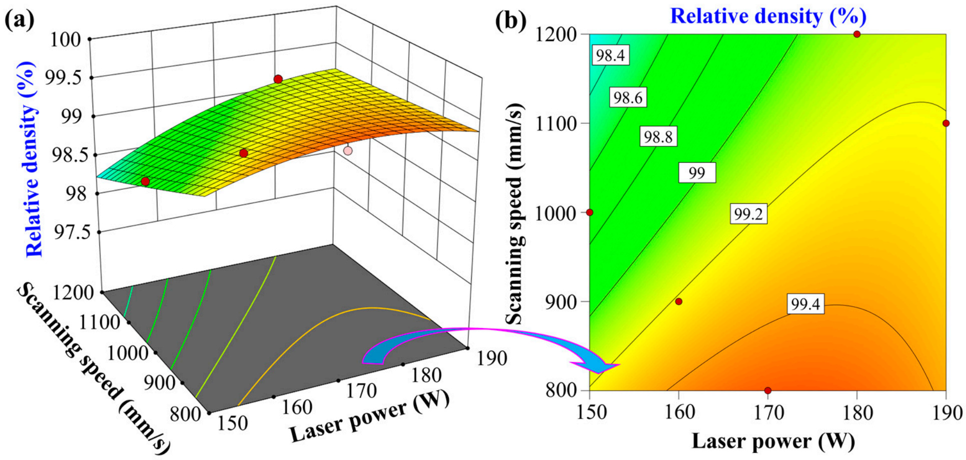

Figure 7. Response surface graph (**a**) and contour plot (**b**) of the effects of laser power and scanning speed on the relative density at scanning interval of 0.08 mm.

Here, P represents the laser power (W), v refers to the laser scanning speed (mm/s), h is the laser scanning interval (mm), and t is the layer thickness (mm), which remains at 0.03 mm throughout the investigation. Based on Equation (2), the E_v of each sample is listed in Table 3.

Figure 8 indicates the correlation between volume energy density and relative density of the TA15 alloy fabricated via LPBF processes. It can be found from Figure 8 that a lower relative density of 98.24% occurred at a lower energy density of 48.48 J/mm^3, which was due to the low level of laser energy input not being able to make the powder surface melt completely, resulting in the lack of fusion, as shown in Figure 9a. Thus, a higher energy density could be utilized to realize higher values of relative density. When the laser energy density was adjusted to 100 J/mm^3, the highest relative density could reach 99.7%, as shown in Table 3. There are almost no defects such as pores, as indicated in (Figure 9b). Notably, the further increase in the energy input would lead slightly to the reduction in the relative density due to the vaporization of material caused by the high absorption of heat from melt pool turbulence or the interaction zone [36], which would result in the formation of tiny holes, as shown in Figure 9c.

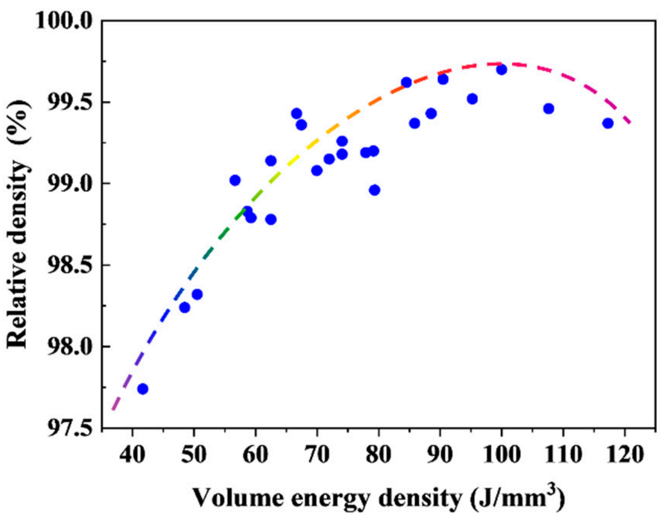

Figure 8. Relationship between relative density and volume energy density for LPBF-fabricated TA15 titanium alloy.

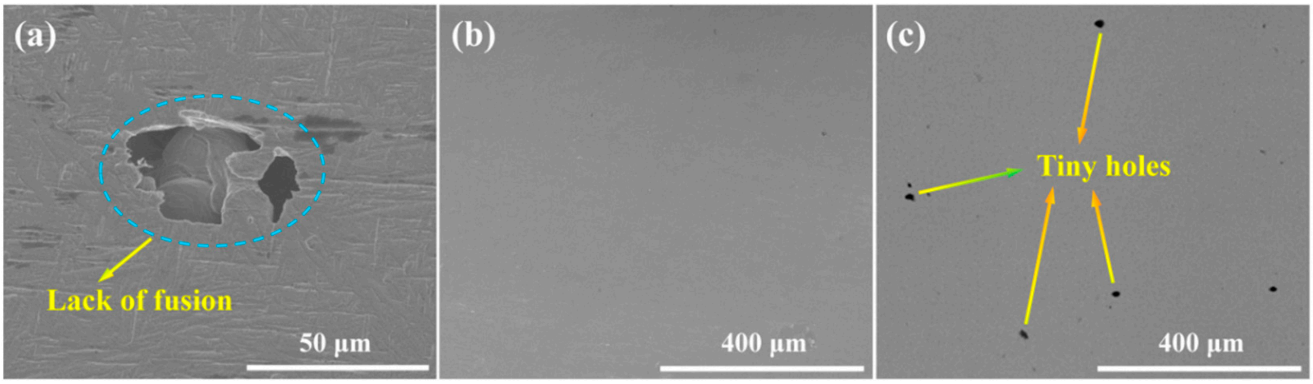

Figure 9. Various types of defects present across the as-LPBFed TA15 titanium alloy at different energy densities: (**a**) 48.48 J/mm^3, (**b**) 100 J/mm^3, and (**c**) 117.28 J/mm^3.

3.4. Confirmation Analysis

In order to better reveal the correlation between relative density and laser power, and scanning speed and scanning interval, the regression analysis was carried out for relative density. With the regression expression given according to the response parameter (relative density) and the three input process parameters (laser power (A), scanning speed (B), and scanning interval (C)) with the expression via a second-order polynomial, the equation is as follows [50]:

$$\text{Relative density} = a_0 + a_1(A) + a_2(B) + a_3(C) + a_4(AB) + a_5(AC) + a_6(BC) + a_7(ABC) \quad (3)$$

Table 7 shows the corresponding value of coefficients from a_0 to a_7 for the relative density. By replacing each value of these three process parameters and corresponding coefficients in the regression expression, the predicted value for relative density could be obtained. Recall above Table 3 that the values of prediction and experiment for relative density were clearly shown, and the values of prediction and experiment for relative density were compared. The result indicates that the difference between their values was not remarkable and their percentage of error was less than 0.5%. The confirmation analysis had been finished to identify that the values of prediction and experiment obtained by means of the regression equation were nearly the same. Directly, the high correlation between experimental values and predicted values for relative density is directly shown in Figure 10.

Table 7. The regression equation coefficients for relative density.

Coefficient	The Corresponding Value
a_0	111.61
a_1	-1.06×10^{-1}
a_2	-1.64×10^{-2}
a_3	5.23
a_4	1.35×10^{-4}
a_5	4.91×10^{-1}
a_6	1.89×10^{-2}
a_7	-7.18×10^{-4}

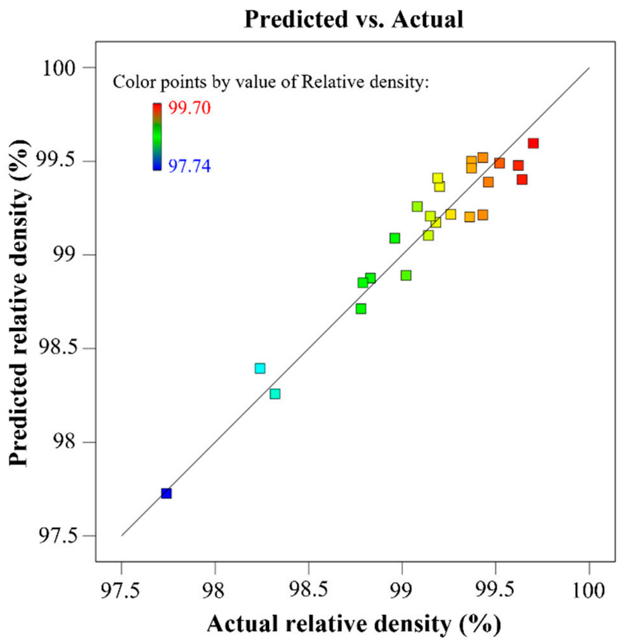

Figure 10. Correlation graph of the experimental values and predicted values of relative density.

4. Conclusions

(1) With the increase in laser power, the relative density first increased and then decreased. When the laser power was 180 W, the relative density could reach the peak value of 99.5%. However, the higher laser power of 190 W caused the decrease in relative density, which was owing to the excessive energy input to the elements by burning, resulting in the decrease in relative density.

(2) As the scanning interval increased from 0.06 mm to 0.10 mm with an interval of 0.01 mm, the density of the as-LPBFed TA15 titanium alloy decreased correspondingly from 99.41% to 98.72% with a smooth trend. The descent trend of density with increasing scanning interval was owing to the lower energy density per unit volume, causing the decreased energy absorbed by the TA15 powders.

(3) The correlation between relative density, laser power, scanning speed, and scanning interval was analyzed by the regression expression (A: laser power, B: scanning speed, and C: scanning interval) as follows:

Relative density = $111.61 - 1.06 \times 10^{-1}$ (A) $- 1.64 \times 10^{-2}$ (B) + 5.23 (C) + 1.35×10^{-4} (AB) + 4.91×10^{-1} (AC) + 1.89×10^{-2} (BC) $- 7.18 \times 10^{-4}$ (ABC)

Author Contributions: Conceptualization, Z.W. and Q.W.; methodology, Q.W. and L.Z.; validation, Y.S., X.S. and X.Z. (Xuefeng Zhang); formal analysis, L.Z. and Q.W.; investigation, Q.W., X.Z. (Xichen Zhang) and W.G.; resources, Y.L., X.S. and X.Z. (Xuefeng Zhang); data curation, Z.W. and J.X.; writing—original draft, Z.W. and Q.W.; writing—review and editing, Y.L., Y.S. and X.S.; supervision, L.Z. and X.Z. (Xuefeng Zhang); project administration, Y.L.; funding acquisition, Y.L. and X.Z. (Xuefeng Zhang). All authors have read and agreed to the published version of the manuscript.

Funding: This research was funded by the Natural Science Foundation of Zhejiang Province (2021C01023), Natural Science Foundation of China (52105334), Natural Science Foundation of Hunan Province of China (2021JJ40206, 2022JJ20025), Key Research and Development Program of Hunan Province of China (2022GK2043), and Education Department of Jilin Province (JJKH20210733KJ).

Institutional Review Board Statement: Not applicable.

Informed Consent Statement: Not applicable.

Data Availability Statement: The data presented in this study are available on request from the corresponding author.

Conflicts of Interest: The authors declare no conflict of interest.

References

1. Wang, C.S.; Li, C.L.; Chen, R.; Qin, H.Z.; Ma, L.; Mei, Q.S.; Zhang, G.D. Multistep Low-to-High-Temperature Heating as a Suitable Alternative to Hot Isostatic Pressing for Improving Laser Powder-Bed Fusion-Fabricated Ti-6Al-2Zr-1Mo-1V Microstructural and Mechanical Properties. *Mater. Sci. Eng. A* **2022**, *841*, 143022. [CrossRef]
2. Huang, S.; Sun, B.; Guo, S. Microstructure and Property Evaluation of TA15 Titanium Alloy Fabricated by Selective Laser Melting after Heat Treatment. *Opt. Laser Technol.* **2021**, *144*, 107422. [CrossRef]
3. Li, S.; Lan, X.; Wang, Z.; Mei, S. Microstructure and Mechanical Properties of Ti-6.5Al-2Zr-Mo-V Alloy Processed by Laser Powder Bed Fusion and Subsequent Heat Treatments. *Addit. Manuf.* **2021**, *48*, 102382. [CrossRef]
4. Takase, A.; Ishimoto, T.; Morita, N.; Ikeo, N.; Nakano, T. Comparison of Phase Characteristics and Residual Stresses in Ti-6al-4v Alloy Manufactured by Laser Powder Bed Fusion (L-Pbf) and Electron Beam Powder Bed Fusion (Eb-Pbf) Techniques. *Crystals* **2021**, *11*, 796. [CrossRef]
5. Zhang, Y.; Zhang, S.; Zou, Z.; Shi, Y. Achieving an Ideal Combination of Strength and Plasticity in Additive Manufactured Ti–6.5Al–2Zr–1Mo–1V Alloy through the Development of Tri-Modal Microstructure. *Mater. Sci. Eng. A* **2022**, *840*, 142944. [CrossRef]
6. Zhang, S.; Zhang, Y.; Zou, Z.; Shi, Y.; Zang, Y. The Microstructure and Tensile Properties of Additively Manufactured Ti–6Al–2Zr–1Mo–1V with a Trimodal Microstructure Obtained by Multiple Annealing Heat Treatment. *Mater. Sci. Eng. A* **2022**, *831*, 142241. [CrossRef]
7. Hu, M.; Wang, L.; Li, G.; Huang, Q.; Liu, Y.; He, J.; Wu, H.; Song, M. Investigations on Microstructure and Properties of Ti-Nb-Zr Medium-Entropy Alloys for Metallic Biomaterials. *Intermetallics* **2022**, *145*, 107568. [CrossRef]
8. Tao, P.; Shao, H.; Ji, Z.; Nan, H.; Xu, Q. Numerical Simulation for the Investment Casting Process of a Large-Size Titanium Alloy Thin-Wall Casing. *Prog. Nat. Sci. Mater. Int.* **2018**, *28*, 520–528. [CrossRef]
9. Uwanyuze, R.S.; Kanyo, J.E.; Myrick, S.F.; Schafföner, S. A Review on Alpha Case Formation and Modeling of Mass Transfer during Investment Casting of Titanium Alloys. *J. Alloys Compd.* **2021**, *865*, 158558. [CrossRef]
10. Sun, Z.C.; Zhang, J.; Yang, H.; Wu, H.L. Effect of Workpiece Size on Microstructure Evolution of Different Regions for TA15 Ti-Alloy Isothermal near-β Forging by Local Loading. *J. Mater. Process. Technol.* **2015**, *222*, 234–243. [CrossRef]
11. Zhang, R.; Wang, D.J.; Yuan, S.J. Effect of Multi-Directional Forging on the Microstructure and Mechanical Properties of TiBw/TA15 Composite with Network Architecture. *Mater. Des.* **2017**, *134*, 250–258. [CrossRef]
12. Liu, W.; Sheng, Q.; Ma, Y.; Cai, Q.; Wang, J.; Liu, Y. Interfacial Microstructures, Residual Stress and Mechanical Analysis of Hot Isostatic Pressing Diffusion Bonded Joint of 93W–4.9Ni–2.1Fe Alloy and 30CrMnSiNi2A Steel. *Fusion Eng. Des.* **2020**, *156*, 111602. [CrossRef]
13. Li, J.; Shen, J.; Hu, S.; Zhang, H.; Bu, X. Microstructure and Mechanical Properties of Ti-22Al-25Nb/TA15 Dissimilar Joint Fabricated by Dual-Beam Laser Welding. *Opt. Laser Technol.* **2019**, *109*, 123–130. [CrossRef]
14. Wang, C.; Guo, Q.; Shao, M.; Zhang, H.; Wang, F.; Song, B.; Ji, Y.; Li, H. Microstructure and Corrosion Behavior of Linear Friction Welded TA15 and TC17 Dissimilar Joint. *Mater. Charact.* **2022**, *187*, 111871. [CrossRef]
15. Samal, S.K.; Vishwanatha, H.M.; Saxena, K.K.; Behera, A.; Nguyen, T.A.; Behera, A.; Prakash, C.; Dixit, S.; Mohammed, K.A. 3D-Printed Satellite Brackets: Materials, Manufacturing and Applications. *Crystals* **2022**, *12*, 1148. [CrossRef]
16. Liu, C.; Liu, Y.; Wang, T.; Liu, W.; Ma, Y. Effects of Heat Treatment on the Microstructure and Properties of Graded-Density Powder Aluminum Alloys. *Met. Sci. Heat Treat.* **2022**, *63*, 590–598. [CrossRef]
17. Song, X.; Zhang, K.; Song, Y.; Duan, Z.; Liu, Q.; Liu, Y. Morphology, Microstructure and Mechanical Properties of Electrospun Alumina Nanofibers Prepared Using Different Polymer Templates: A Comparative Study. *J. Alloys Compd.* **2020**, *829*, 154502. [CrossRef]
18. Wen, Z.; Song, X.; Chen, D.; Fan, T.; Liu, Y.; Cai, Q. Electrospinning Preparation and Microstructure Characterization of Homogeneous Diphasic Mullite Ceramic Nanofibers. *Ceram. Int.* **2020**, *46*, 12172–12179. [CrossRef]
19. Song, Y.; Ding, X.; Xiao, L.; Liu, W.; Chen, Y.; Zhao, X. The Effect of Ni Plating on the Residual Stress and Micro-Yield Strength in an Al-Cu-Mg Alloy Under Different Diffusion Treatments. *JOM* **2019**, *71*, 4370–4377. [CrossRef]
20. Xiao, L.R.; Tu, X.X.; Zhao, X.J.; Cai, Z.Y.; Song, Y.F. Microstructural Evolution and Dimensional Stability of TiC-Reinforced Steel Matrix Composite during Tempering. *Mater. Lett.* **2020**, *259*, 8–12. [CrossRef]
21. Song, Y.F.; Ding, X.F.; Zhao, X.J.; Xiao, L.R.; Yu, C.X. The Effect of SiC Addition on the Dimensional Stability of Al-Cu-Mg Alloy. *J. Alloys Compd.* **2018**, *750*, 111–116. [CrossRef]
22. Tang, X.; Din, C.; Yu, S.; Liu, Y.; Luo, H.; Zhang, D.; Chen, S. Synthesis of Dielectric Polystyrene via One-Step Nitration Reaction for Large-Scale Energy Storage. *Chem. Eng. J.* **2022**, *446*, 137281. [CrossRef]
23. Yu, S.; Ding, C.; Liu, Y.; Liu, Y.; Zhang, Y.; Luo, H.; Zhang, D.; Chen, S. Enhanced Breakdown Strength and Energy Density over a Broad Temperature Range in Polyimide Dielectrics Using Oxidized MXenes Filler. *J. Power Sources* **2022**, *535*, 231415. [CrossRef]
24. Cai, C.; Wu, X.; Liu, W.; Zhu, W.; Chen, H.; Qiu, J.C.D.; Sun, C.N.; Liu, J.; Wei, Q.; Shi, Y. Selective Laser Melting of Near-α Titanium Alloy Ti-6Al-2Zr-1Mo-1V: Parameter Optimization, Heat Treatment and Mechanical Performance. *J. Mater. Sci. Technol.* **2020**, *57*, 51–64. [CrossRef]
25. Xu, J.; Wu, Z.; Niu, J.; Song, Y.; Liang, C.; Yang, K.; Chen, Y.; Liu, Y. Effect of Laser Energy Density on the Microstructure and Microhardness of Inconel 718 Alloy Fabricated by Selective Laser Melting. *Crystals* **2022**, *12*, 1243. [CrossRef]

26. Yang, H.; Liu, B.; Niu, P.; Fan, Z.; Yuan, T.; Wang, Y.; Liu, Y.; Li, R. Effect of Laser Scanning Angle on Shear Slip Behavior along Melt Track of Selective Laser Melted 316l Stainless Steel during Tensile Failure. *Mater. Charact.* **2022**, *193*, 112297. [CrossRef]
27. Liu, Y.; Liu, W.; Ma, Y.; Liang, C.; Liu, C.; Zhang, C.; Cai, Q. Microstructure and Wear Resistance of Compositionally Graded Ti–Al Intermetallic Coating on Ti6Al4V Alloy Fabricated by Laser Powder Deposition. *Surf. Coat. Technol.* **2018**, *353*, 32–40. [CrossRef]
28. Liu, Y.; Liu, C.; Liu, W.; Ma, Y.; Zhang, C.; Cai, Q.; Liu, B. Microstructure and Properties of Ti/Al Lightweight Graded Material by Direct Laser Deposition. *Mater. Sci. Technol.* **2018**, *34*, 945–951. [CrossRef]
29. Liu, Y.; Wu, Z.; Liu, W.; Ma, Y. Microstructure Evolution and Reaction Mechanism of Continuously Compositionally Ti/Al Intermetallic Graded Material Fabricated by Laser Powder Deposition. *J. Mater. Res. Technol.* **2022**, *20*, 4173–4185. [CrossRef]
30. Li, R.; Wang, H.; He, B.; Li, Z.; Zhu, Y.; Zheng, D.; Tian, X.; Zhang, S. Effect of α Texture on the Anisotropy of Yield Strength in Ti–6Al–2Zr–1Mo–1V Alloy Fabricated by Laser Directed Energy Deposition Technique. *Mater. Sci. Eng. A* **2021**, *824*, 141771. [CrossRef]
31. Li, R.; Wang, H.; Zheng, D.; Gao, X.; Zhang, S. Texture Evolution during Sub-Critical Annealing and Its Effect on Yield Strength Anisotropy of Laser Directed Energy Deposited Ti-6Al-2Zr-1Mo-1V Alloy. *Mater. Sci. Eng. A* **2022**, *850*, 143556. [CrossRef]
32. Abd-elaziem, W.; Elkatatny, S.; Abd-elaziem, A.; Khedr, M.; El-baky, M.A.A.; Ali Hassan, M.; Abu-Okail, M.; Mohammed, M. On the Current Research Progress of Metallic Materials Fabricated by Laser Powder Bed Fusion Process: A Review. *J. Mater. Res. Technol.* **2022**, *20*, 681–707. [CrossRef]
33. Wu, X.; Zhang, D.; Guo, Y.; Zhang, T.; Liu, Z. Microstructure and Mechanical Evolution Behavior of LPBF (Laser Powder Bed Fusion)-Fabricated TA15 Alloy. *J. Alloys Compd.* **2021**, *873*, 159639. [CrossRef]
34. Yao, Z.; Yang, T.; Yang, M.; Jia, X.; Wang, C.; Yu, J.; Li, Z.; Han, H.; Liu, W.; Xie, G.; et al. Martensite Colony Engineering: A Novel Solution to Realize the High Ductility in Full Martensitic 3D-Printed Ti Alloys. *Mater. Des.* **2022**, *215*, 110445. [CrossRef]
35. Liu, Y.; Liang, C.; Liu, W.; Ma, Y.; Liu, C.; Zhang, C. Dilution of Al and V through Laser Powder Deposition Enables a Continuously Compositionally Ti/Ti6Al4V Graded Structure. *J. Alloys Compd.* **2018**, *763*, 376–383. [CrossRef]
36. King, W.E.; Barth, H.D.; Castillo, V.M.; Gallegos, G.F.; Gibbs, J.W.; Hahn, D.E.; Kamath, C.; Rubenchik, A.M. Observation of Keyhole-Mode Laser Melting in Laser Powder-Bed Fusion Additive Manufacturing. *J. Mater. Process. Technol.* **2014**, *214*, 2915–2925. [CrossRef]
37. Wang, W.; Liang, S.Y. Physics-Based Predictive Model of Lack-of-Fusion Porosity in Laser Powder Bed Fusion Considering Cap Area. *Crystals* **2021**, *11*, 1568. [CrossRef]
38. Chowdhury, S.; Yadaiah, N.; Prakash, C. Laser Powder Bed Fusion: A State-of-the-Art Review of the Technology, Materials, Properties & Defects and Numerical Modelling. *J. Mater. Res. Technol.* **2022**, *20*, 2109–2172. [CrossRef]
39. Li, S.; Yang, J.; Wang, Z. Multi-Laser Powder Bed Fusion of Ti-6.5Al-2Zr-Mo-V Alloy Powder: Defect Formation Mechanism and Microstructural Evolution. *Powder Technol.* **2021**, *384*, 100–111. [CrossRef]
40. Thijs, L.; Verhaeghe, F.; Craeghs, T.; Humbeeck, J.V.; Kruth, J.P. A Study of the Microstructural Evolution during Selective Laser Melting of Ti-6Al-4V. *Acta Mater.* **2010**, *58*, 3303–3312. [CrossRef]
41. Liu, Y.; Liu, C.; Liu, W.; Ma, Y.; Tang, S.; Liang, C.; Cai, Q.; Zhang, C. Optimization of Parameters in Laser Powder Deposition AlSi10Mg Alloy Using Taguchi Method. *Opt. Laser Technol.* **2019**, *111*, 470–480. [CrossRef]
42. Jiang, H.Z.; Li, Z.Y.; Feng, T.; Wu, P.Y.; Chen, Q.S.; Feng, Y.L.; Li, S.W.; Gao, H.; Xu, H.J. Factor Analysis of Selective Laser Melting Process Parameters with Normalised Quantities and Taguchi Method. *Opt. Laser Technol.* **2019**, *119*, 105592. [CrossRef]
43. Canel, T.; Zeren, M.; Sınmazçelik, T. Laser Parameters Optimization of Surface Treating of Al 6082-T6 with Taguchi Method. *Opt. Laser Technol.* **2019**, *120*, 105714. [CrossRef]
44. Kumar, R.; Katyal, P.; Mandhania, S. Grey Relational Analysis Based Multiresponse Optimization for WEDM of ZE41A Magnesium Alloy. *Int. J. Light. Mater. Manuf.* **2022**, *5*, 543–554. [CrossRef]
45. Pandel, D.; Kumar Singh, A.; Kumar Banerjee, M.; Gupta, R. Optimization of Mg2(Si-Sn) Based Thermoelectric Generators Using the Taguchi Method. *Mater. Today Proc.* **2020**, *44*, 4124–4130. [CrossRef]
46. Liu, Y.; Liu, C.; Liu, W.; Ma, Y.; Zhang, C.; Liang, C.; Cai, Q. Laser Powder Deposition Parametric Optimization and Property Development for Ti-6Al-4V Alloy. *J. Mater. Eng. Perform.* **2018**, *27*, 5613–5621. [CrossRef]
47. Wei, M.; Chen, S.; Liang, J.; Liu, C. Effect of Atomization Pressure on the Breakup of TA15 Titanium Alloy Powder Prepared by EIGA Method for Laser 3D Printing. *Vacuum* **2017**, *143*, 185–194. [CrossRef]
48. Li, Y.; Hu, Y.; Cong, W.; Zhi, L.; Guo, Z. Additive Manufacturing of Alumina Using Laser Engineered Net Shaping: Effects of Deposition Variables. *Ceram. Int.* **2017**, *43*, 7768–7775. [CrossRef]
49. Jiang, J.; Chen, J.; Ren, Z.; Mao, Z.; Ma, X.; Zhang, D.Z. The Influence of Process Parameters and Scanning Strategy on Lower Surface Quality of TA15 Parts Fabricated by Selective Laser Melting. *Metals* **2020**, *10*, 1228. [CrossRef]
50. Read, N.; Wang, W.; Essa, K.; Attallah, M.M. Selective Laser Melting of AlSi10Mg Alloy: Process Optimisation and Mechanical Properties Development. *Mater. Des.* **2015**, *65*, 417–424. [CrossRef]